Journal of ELECTRONIC MATERIALS, Vol. 47, No. 1, 2018
DOI: 10.1007/s11664-017-5751-y

Finite Element Study on Performance of Piezoelectric Bimorph Cantilevers Using Porous/Ceramic 0–3 Polymer Composites

RAJ KIRAN,[1] ANURUDDH KUMAR,[1] VISHAL S. CHAUHAN,[1] RAJEEV KUMAR,[1] and RAHUL VAISH[1,2]

1.—School of Engineering, Indian Institute of Technology Mandi, Mandi, H.P. 175005, India. 2.—e-mail: rahul@iitmandi.ac.in

Finite element analysis of 0–3 composites made of piezoceramic particles and pores embedded in polyvinylidene difluoride (PVDF) has been carried out. The representative volume element (RVE) approach was used to calculate the effective elastic and piezoelectric properties of the periodic isotropic 0–3 piezoelectric composites. It was observed that the elastic and piezoelectric properties increased with the volume fraction of $K_{0.475}Na_{0.475}Li_{0.05}(Nb_{0.92}Ta_{0.05}Sb_{0.03})O_3$ (KNLNTS) particles but decreased for the porous composites. These effective properties were further used to analyze the potential use of such bimorph cantilever beams in sensing and energy harvesting applications. Sensing voltage continuously increased for KNLNTS filled composites while for porous materials it increased up to 15% volume fraction porosity and then decreased. The same trend was also observed for the power produced by the harvester. However, the sensing voltage and power produced by harvesters made of porous composites were lower than for harvesters made of pure PVDF.

Key words: Piezoelectricity, composites, RVE, porosity, KNLNTS, PVDF

INTRODUCTION

Piezoelectric materials have the unique ability to convert mechanical energy into electrical energy and vice versa,[1] enabling wide use of piezoelectric ceramics in sensing and actuation applications. Despite their superiority over other electromechanical transducers, piezoelectric ceramics are often limited by their weight and high specific acoustic impedance. Bulk piezoelectric materials suffer from several disadvantages, so piezocomposites are better solutions for use in sensing and harvesting applications. Recently, such composites have been developed using combinations of piezoceramics and polymers, being widely used in energy harvesting, vibration control, and smart structures due to their high conformability.[2,3] Newnham et al.[4] found that piezocomposites have higher flexibility due to the polymer matrix and are easier to fabricate than bulk piezoceramics. Generally, unimorph or bimorph structures are used for sensing and actuation applications, where the piezoceramic is embedded into polymer layers and bonded to a substrate.[5–8] At present, the most commonly used piezoceramics are from the lead zirconate titanate (PZT) family. However, use of these ceramics is strongly discouraged because of their toxic nature.

This has motivated researchers to explore new directions to identify lead-free piezoceramics with improved or at least comparable physical and dielectric properties. The most promising alternatives to PZT are $K_{0.5}Na_{0.5}NbO_3$ (KNN)-based and $Bi_{0.5}Na_{0.5}TiO_3$ (BNT)-based composites.[9–12] Kothari et al.[13] carried out a comparative study of 1–3 piezoelectric composites and investigated the effective properties and performance of different lead-free materials including PZT-5A. In present study, KNLNTS was taken as a lead-free material, as its piezoelectric strain coefficient in transverse mode is higher than that of PZT-5A.[14,15]

Use of lead-free piezoelectric composites in sensors and energy harvesters is very limited in

(Received April 27, 2017; accepted August 16, 2017; published online September 5, 2017)

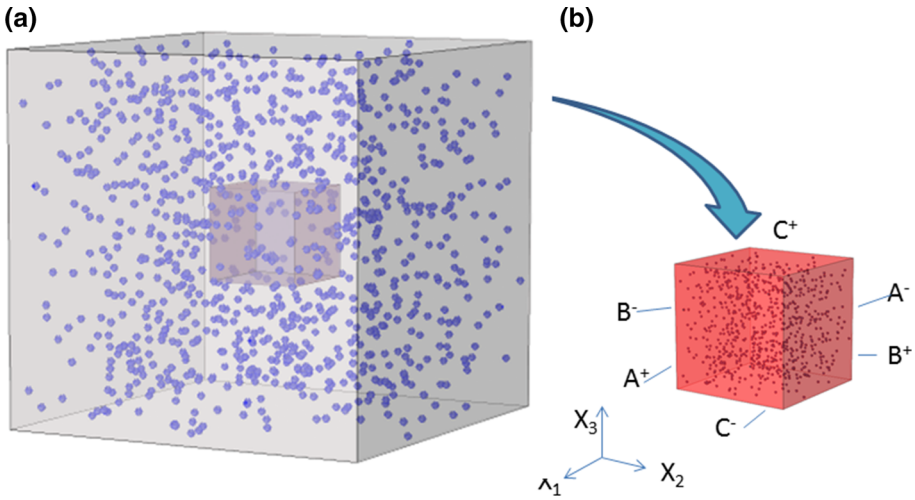

Fig. 1. Schematic diagram of: (a) 0–3 composite; (b) representative volume element and its global coordinate system.

literature, as they have not been studied from the design and application points of view. However, Sharma et al.[16] studied the performance of lead-free piezoelectric materials for use in active structural vibration control.

Although a number of studies have been carried out on the effective properties of such composites, most of them were limited to lead-based materials. Gupta et al.[17] investigated the complete electromechanical response for particulate, short-fiber, long-fiber, laminate, and networked composites. Wang et al.[18] conducted experiments on a PZT–cement composite and revealed the dependence on the particle size. Gupta et al.[19] developed a finite element model to study the effect of porosity on the effective electromechanical properties of 1–3 composites. Recently, Ayuso et al.[20] presented a homogenization study on porous piezoelectric materials based on analytical and numerical analyses. Although the effect of fillers and porosity on the effective elastic and piezoelectric properties was considered, the practical application of such materials was neglected in that study. The present study focuses on evaluation of effective properties of KNLNTS-PVDF-based composites and porous PVDF, then investigates the sensing and energy harvesting capability of these materials using a finite element method. As a first step, micromechanical theory was used to evaluate the effective elastic and piezoelectric properties. These properties were further used for dynamic analysis of bimorph cantilever beams to evaluate their sensing and energy harvesting performance.

COMPUTATIONAL PROCEDURES

The effective elastic and piezoelectric properties were computed for lead-free composites of 0–3 type containing $K_{0.475}Na_{0.475}Li_{0.05}(Nb_{0.92}Ta_{0.05}Sb_{0.03})O_3$ (KNLNTS) and porous PVDF, and their application in smart structures was compared. PVDF-based composites were modeled using circular inclusions of KNLNTS with random orientation. Similarly, circular pores were considered in a PVDF matrix in a random fashion. Figure 1a and b shows a typical model of two 0–3 composites and the representative volume element. The materials considered and their properties are listed in Table I.

Finite Element Modeling of 0–3 Piezoelectric Composites

A number of numerical and analytical studies that predict the mechanical and electrical properties of lead-based piezoelectric composites have been reported.[22–26] The analytical methods proposed by Chan and Unsworth[27] and Smith and Auld[28] were insufficient to capture the overall material properties. Berger et al.[15] successfully evaluated the effective material properties of piezoelectric composites using analytical and numerical methods. The asymptotic homogenization method (AHM) was employed to determine the analytical solution,[29,30] while the numerical model was validated by a finite element method. It becomes very difficult to predict the response of composites using analytical methods, as the shape of the inclusions becomes complex. Therefore, numerical methods such as FEM are used. Many authors such as Poizat and Sester,[22] Gaudenzi,[24] and Teply and Dvorak[31] have also used FEM to predict effective electromechanical properties.

One of the essential approaches to determine the effective properties of a composite is to model the unit cell, also known as the representative volume element. Nemat-Nasser and Hori stated that the RVE for a material point of a continuum is a material volume that is statistically representative of the infinitesimal neighborhood at that material point[32]; It is the smallest volume over which the

Table I. Physical properties of materials

Material	E (GPa)	ν	e_{13} (C/m^2)	e_{15} (C/m^2)	e_{33} (C/m^2)	$\varepsilon_{11}^T/\varepsilon_0$	$\varepsilon_{33}^T/\varepsilon_0$	Ref.
PVDF	2	0.3	0.0104	0.0388	0.065	12	12	21
KNLNTS	87	0.39	16.3	8.4	11.4	613.6	745.8	14

calculation of any material property will yield the same value as over the whole composite. The main idea behind modeling an RVE is to find a homogeneous medium that can represent the original composite as a whole. Berger et al.[33] successfully modeled the RVE and applied suitable boundary conditions to determine various effective properties of piezoelectric composites.

In coupled piezoelectric problems, mechanical strain induces an electric potential gradient in the material, while an electric field results in mechanical deformation, which are commonly known as the direct and converse piezoelectric effect, respectively. In piezoelectric materials, this coupling between the mechanical and electric fields can be characterized by the piezoelectric coefficients. The constitutive relationship for piezoelectric materials correlating the stress, strain, electric field, and displacement can be expressed in matrix form as follows[15]:

$$\begin{bmatrix} \bar{T}_{11} \\ \bar{T}_{22} \\ \bar{T}_{33} \\ \bar{T}_{23} \\ \bar{T}_{31} \\ \bar{T}_{12} \\ \bar{D}_1 \\ \bar{D}_2 \\ \bar{D}_3 \end{bmatrix} = \begin{bmatrix} C_{11}^{\text{eff}} & C_{12}^{\text{eff}} & C_{13}^{\text{eff}} & 0 & 0 & 0 & 0 & 0 & -e_{13}^{\text{eff}} \\ C_{12}^{\text{eff}} & C_{11}^{\text{eff}} & C_{13}^{\text{eff}} & 0 & 0 & 0 & 0 & 0 & -e_{13}^{\text{eff}} \\ C_{13}^{\text{eff}} & C_{13}^{\text{eff}} & C_{33}^{\text{eff}} & 0 & 0 & 0 & 0 & 0 & -e_{33}^{\text{eff}} \\ 0 & 0 & 0 & C_{44}^{\text{eff}} & 0 & 0 & 0 & -e_{15}^{\text{eff}} & 0 \\ 0 & 0 & 0 & 0 & C_{44}^{\text{eff}} & 0 & -e_{15}^{\text{eff}} & 0 & 0 \\ 0 & 0 & 0 & 0 & 0 & C_{66}^{\text{eff}} & 0 & 0 & 0 \\ 0 & 0 & 0 & 0 & e_{15}^{\text{eff}} & 0 & \varepsilon_{11}^{\text{eff}} & 0 & 0 \\ 0 & 0 & 0 & e_{15}^{\text{eff}} & 0 & 0 & 0 & \varepsilon_{11}^{\text{eff}} & 0 \\ e_{13}^{\text{eff}} & e_{13}^{\text{eff}} & e_{33}^{\text{eff}} & 0 & 0 & 0 & 0 & 0 & \varepsilon_{33}^{\text{eff}} \end{bmatrix} \begin{bmatrix} \bar{S}_{11} \\ \bar{S}_{22} \\ \bar{S}_{33} \\ \bar{S}_{23} \\ \bar{S}_{31} \\ \bar{S}_{12} \\ \bar{E}_1 \\ \bar{E}_2 \\ \bar{E}_3 \end{bmatrix}, \tag{1}$$

where $\bar{T}_{ij}$, $\bar{D}_i$, $\bar{S}_{ij}$, and $\bar{E}_i$ denote the average values of engineering stress, electrical displacement, engineering strain, and electric potential, respectively.

For micromechanical analysis, composites can be studied using the representative volume element.[34] Since the RVE determines the effective properties of composites, the accuracy of such results largely depends on the choice of the RVE.[35] In the present study, the inclusions are considered to be perfectly bonded to the matrix and modeled as isotropic spheres. The matrix and inclusions are both uniformly poled along the x_3 direction. Electromechanical coupling is considered by including an electric potential degree of freedom along with displacement in the analyses.

Periodic Boundary Conditions for the RVE

Since composite materials can be represented as a periodic array of RVEs to simulate the response of the whole composite, periodic boundary conditions must be imposed on the RVE. These boundary conditions ensure that each RVE has the same deformation mode, with no penetration or separation between neighboring RVEs. These boundary conditions on the RVE surfaces can be described in Cartesian coordinates as follows[22,34,36–38]:

$$u_i = \bar{S}_{ij}x_i + v_i, \tag{2}$$

where $\bar{S}_{ij}$ are the average engineering strains, and w_i is the local fluctuation or periodic part of the displacement components on the boundary surfaces, generally being unknown and depending on the applied global load. The indices i and j denote the global three-dimensional coordinate directions in the range from 1 to 3. A more precise expression for the displacements on a pair of opposite boundary surfaces (with normal along x_j axis) is

$$u_i^{K^+} = \bar{S}_{ij}x_j^{K^+} - v_i^{K^+}, \tag{3}$$

$$u_i^{K^-} = \bar{S}_{ij}x_j^{K^-} - v_i^{K^-}, \tag{4}$$

where the index K^+ denotes along the positive x_j direction and K^- denotes the negative x_j direction on the faces A^-/A^+, B^-/B^+, and C^-/C^+. Due to the periodic boundary conditions, the local fluctuations $v_i^{K^+}$ and $v_i^{K^-}$ around the average macroscopic value are identical on two opposing surfaces. Thus, the difference between the two equations above gives the applied macroscopic strain condition as[39]

$$u_i^{K^+} - u_i^{K^-} = \bar{S}_{ij}(x_j^{K^+} - x_j^{K^-}). \tag{5}$$

Similarly, the periodic boundary conditions for the electric potential can be given as

$$\phi^{K^+} - \phi^{K^-} = \bar{E}_i(x_i^{K^+} - x_i^{K^-}). \tag{6}$$

The properties of the bulk materials were calculated by averaging the relevant stress and strain values over the RVE using the following equations:

$$\bar{S}_{ij} = \frac{1}{V}\int_V S_{ij}\mathrm{d}V, \tag{7}$$

$$\bar{T}_{ij} = \frac{1}{V}\int_V T_{ij}\mathrm{d}V, \tag{8}$$

where V is the volume of the RVE. Similarly, the average electric fields and electrical displacements are defined as

$$\bar{E}_i = \frac{1}{V}\int_V E_i\mathrm{d}V, \tag{9}$$

$$\bar{D}_i = \frac{1}{V}\int_V D_i\mathrm{d}V. \tag{10}$$

Table II. Boundary conditions and equations for calculation of effective coefficients

Eff. Coeff.	A^- u_i/ϕ	A^+ u_i/ϕ	B^- u_i/ϕ	B^+ u_i/ϕ	C^- u_i/ϕ	C^+ u_i/ϕ	Formula
C_{11}^{eff}	0/–	u_1/0	0/–	0/–	0/0	0/0	$\bar{T}_{11}/\bar{S}_{11}$
C_{12}^{eff}	0/–	u_1/0	0/–	0/–	0/0	0/0	$\bar{T}_{22}/\bar{S}_{11}$
C_{13}^{eff}	0/–	0/–	0/–	0/–	0/0	u_3/–	$\bar{T}_{11}/\bar{S}_{33}$
C_{33}^{eff}	0/–	0/–	0/–	0/–	0/0	u_3/–	$\bar{T}_{33}/\bar{S}_{33}$
C_{44}^{eff}	u_3/0	u_3/0	0/–	0/–	u_1/–	u_1/–	$\bar{T}_{13}/\bar{S}_{31}$
C_{66}^{eff}	u_2/–	u_2/–	u_1/–	u_1/–	0/0	0/0	$\bar{T}_{13}/\bar{S}_{31}$
e_{13}^{eff}	0/–	0/–	0/–	0/–	0/0	0/ϕ	$-\bar{T}_{11}/\bar{S}_3$
e_{33}^{eff}	0/–	0/–	0/–	0/–	0/0	0/ϕ	$\bar{T}_{33}/\bar{E}_3$
e_{15}^{eff}	u_3/0	u_3/0	0/–	0/–	u_1/–	u_1/–	$\bar{D}_1/\bar{S}_{31}$
$\varepsilon_{11}^{\text{eff}}$	0/0	0/ϕ	0/–	0/–	0/–	0/–	$\bar{D}_1/\bar{E}_1$
$\varepsilon_{33}^{\text{eff}}$	0/–	0/–	0/–	0/–	0/0	0/ϕ	$\bar{D}_1/\bar{E}_1$

The homogenized effective properties can be calculated by application of periodic boundary conditions on the opposite faces of the RVE, as described by Eqs. 5 and 6. To predict the effective properties, boundary conditions are applied such that, for a particular load case, there is only a single parameter in the strain/electric field which is nonzero while the others are zero. Since the effective properties are dependent only on the particle volume fraction, the size of the RVE can be chosen as unity. All the dimensions of the RVE are kept at unity, with one corner at the origin. Subsequently, the different coefficients were computed using the boundary conditions described in Table II.

1. Calculation of effective elastic constants (C_{11}^{eff} and C_{12}^{eff})

   The effective elastic constants C_{11}^{eff} and C_{12}^{eff} can be computed by applying boundary conditions such that only mechanical strain in the first direction is nonzero while the mechanical strain and electric potential gradient in all other directions are zero. Now, considering the first and second row of the constitutive Eq. 1, we get

   $$C_{11}^{\text{eff}} = \bar{T}_{11}/\bar{S}_{11} \tag{11}$$

   and

   $$C_{12}^{\text{eff}} = \bar{T}_{22}/\bar{S}_{11}. \tag{12}$$

2. Calculation of effective elastic constants (C_{13}^{eff} and C_{33}^{eff})

   To calculate the effective elastic constants C_{13}^{eff} and C_{33}^{eff}, displacement boundary conditions are applied such that strains are induced in the x_3 direction only. Also, the electric potential gradient on all surfaces should be zero. Now, considering the first and third rows of the constitutive Eq. 2, we get

   $$C_{13}^{\text{eff}} = \bar{T}_{11}/\bar{S}_{33} \tag{13}$$

   and

   $$C_{33}^{\text{eff}} = \bar{T}_{33}/\bar{S}_{33}. \tag{14}$$

3. Calculation of effective elastic constants (C_{44}^{eff} and C_{66}^{eff})

   These coefficients are based on the averaged shear strain and can be calculated by creating a pure shear condition. For these cases, constraint equations (coupling constraints) on two pairs of opposite surfaces must be defined. For C_{44}^{eff}, which is based on the pure in-plane ($x_1 - x_3$ plane) shear state, the constraint equation for a pair of nodes on the opposite surfaces A^-/A^+ can be written as

   $$u_3^{A^+} = u_3^{A^-} + \bar{S}_{31}(x_1^{A^+} - x_1^{A^-}). \tag{15}$$

   The fluctuation $\bar{S}_{31}(x_1^{A^+} - x_1^{A^-})$ can be set to an arbitrary value (unity being used in this study). The analogous constraint equations have to be defined for the opposite surfaces. Similarly, C_{66}^{eff} can also be computed using appropriate boundary conditions.

4. Estimation of effective piezoelectric coefficients (e_{13}^{eff}, e_{33}^{eff}, and e_{15}^{eff}) and dielectric coefficient ($\varepsilon_{33}^{\text{eff}}$)

   The effective piezoelectric coefficients e_{13}^{eff} and e_{33}^{eff} and dielectric coefficient $\varepsilon_{33}^{\text{eff}}$ can be calculated by applying an electric potential gradient in only the x_3 direction while the strains in all directions are zero. Considering rows 6 and 7 of Table II, we get

$$e_{13}^{\text{eff}} = -\bar{T}_{11}/\bar{E}_3, \tag{16}$$

$$e_{33}^{\text{eff}} = -\bar{T}_{33}/\bar{E}_3, \tag{17}$$

and

$$\varepsilon_{33}^{\text{eff}} = \bar{D}_3/\bar{E}_3. \tag{18}$$

The effective coefficient e_{15}^{eff} can be calculated by applying the same shear boundary conditions as applied for finding C_{44}^{eff}. Thereafter, e_{15}^{eff} can be calculated as

$$e_{15}^{\text{eff}} = \bar{D}_1/\bar{S}_{31}. \tag{19}$$

Finite Element Modeling of Piezolaminated Structure for Sensing Application

The finite element method is one of the most effective numerical techniques to determine the response of piezolaminated structures. Different researchers have used the finite element method to analyze the static and dynamic response of piezostructures.[40–44] In the present study, shell elements were used to predict the dynamic response of the structure. Therefore, first-order shear deformation theory and piezoelectric theory were implemented to formulate the shell element. The cantilever beam shown in Fig. 2 was modeled using shell elements. The motivation behind using the shell element is that it is one of the generalized elements and can also be used for structures having curvature. The finite element equations of motion for the piezolaminated shell structure are[45]

$$[M_{uu}]_e\{\ddot{u}\}_e + [C_{uu}]_e\{\dot{u}\}_e + [K_{uu}]_e\{u\}_e + [K_{u\phi}]\{\phi\}_e = \{f^{\text{ext}}\}_e, \tag{20}$$

$$[K_{\phi u}]_e\{u\}_e + [K_{\phi\phi}]_e\{\phi\}_e = \{q^{\text{ext}}\}_e. \tag{21}$$

The generalized element stiffness matrix is given as

$$K_e = \begin{bmatrix} K_{uu} & K_{u\phi} \\ K_{\phi u} & K_{\phi\phi} \end{bmatrix}, \tag{22}$$

where K_{uu} is the mechanical stiffness matrix, $K_{u\phi}$ is the direct piezoelectric coupling matrix, $K_{\phi\phi}$ is the dielectric stiffness matrix, $K_{\phi u}$ is the inverse piezoelectric coupling matrix, u_e is the element nodal displacement vector, ϕ_e is the electric potential vector, f_e^{ext} is the external force vector, and q_e^{ext} is the external electric charge.

Combining Eqs. 20 and 21, the global governing equation can be obtained as[45]

$$[M_{uu}]\{\ddot{u}\} + [C_{uu}]\{\dot{u}\} + [K_{uu}]\{u\} + [K_{u\phi}]\{\phi\} = \{F\}, \tag{23}$$

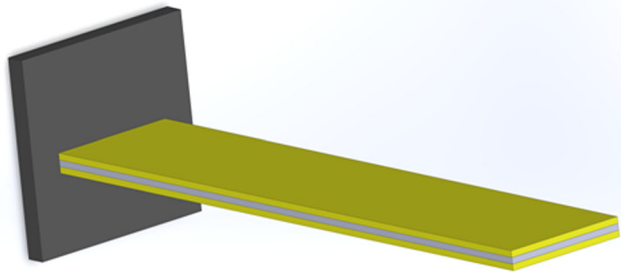

Fig. 2. Schematic of bimorph cantilever beam.

$$[K_{\phi u}]\{u\} + [K_{\phi\phi}]\{\phi\} = \{Q\}. \tag{24}$$

In sensing applications, a piezoelectric material bonded to a substrate acts as the sensor. We now assume that no charge is accumulated on the sensor surface, hence from Eq. 24 the sensor voltage can be deduced as

$$\{\phi\} = -[K_{\phi\phi}]^{-1}[K_{\phi u}]\{u\}. \tag{25}$$

From circuit theory, the current flowing across a resistance due to charge Q is

$$i = -\frac{\mathrm{d}Q}{\mathrm{d}t}. \tag{26}$$

The current across a resistance is given in terms of voltage as

$$i = \frac{V}{R}. \tag{27}$$

From Eq. 21, we have

$$\frac{\mathrm{d}}{\mathrm{d}t}([K_{\phi u}]_e\{u\}_e + [K_{\phi\phi}]_e\{\phi\}_e) = \frac{\mathrm{d}}{\mathrm{d}t}\{Q\}_e, \tag{28}$$

$$[K_{\phi u}]_e\{\dot{r}\}_e + [K_{\phi\phi}]_e\{\dot{v}\}_e = -\frac{\{v\}_e}{R}, \tag{29}$$

$$[K_{\phi u}]_e\{\dot{r}\}_e + [K_{\phi\phi}]_e\{\dot{v}\}_e + \frac{\{v\}_e}{R} = 0. \tag{30}$$

Equations 27 and 30 can then be used to predict the output current and hence calculate the power generated.

To predict the sensing behavior of a piezolaminated structure, a bimorph cantilever beam was modeled, comprising two piezolayers with opposite polarization direction bonded to an aluminum substrate. Composites with different filler volume fraction and porosity were considered for the piezoelectric layers in the beam. A clamped bimorph beam was considered for the sensing application, as shown in Fig. 2. The externally applied electric potential was kept at zero to study the sensing behavior of the piezolayers. A tip load was applied as boundary condition. The mechanical deformation leads to electric displacement and thus charge induction on the terminals.

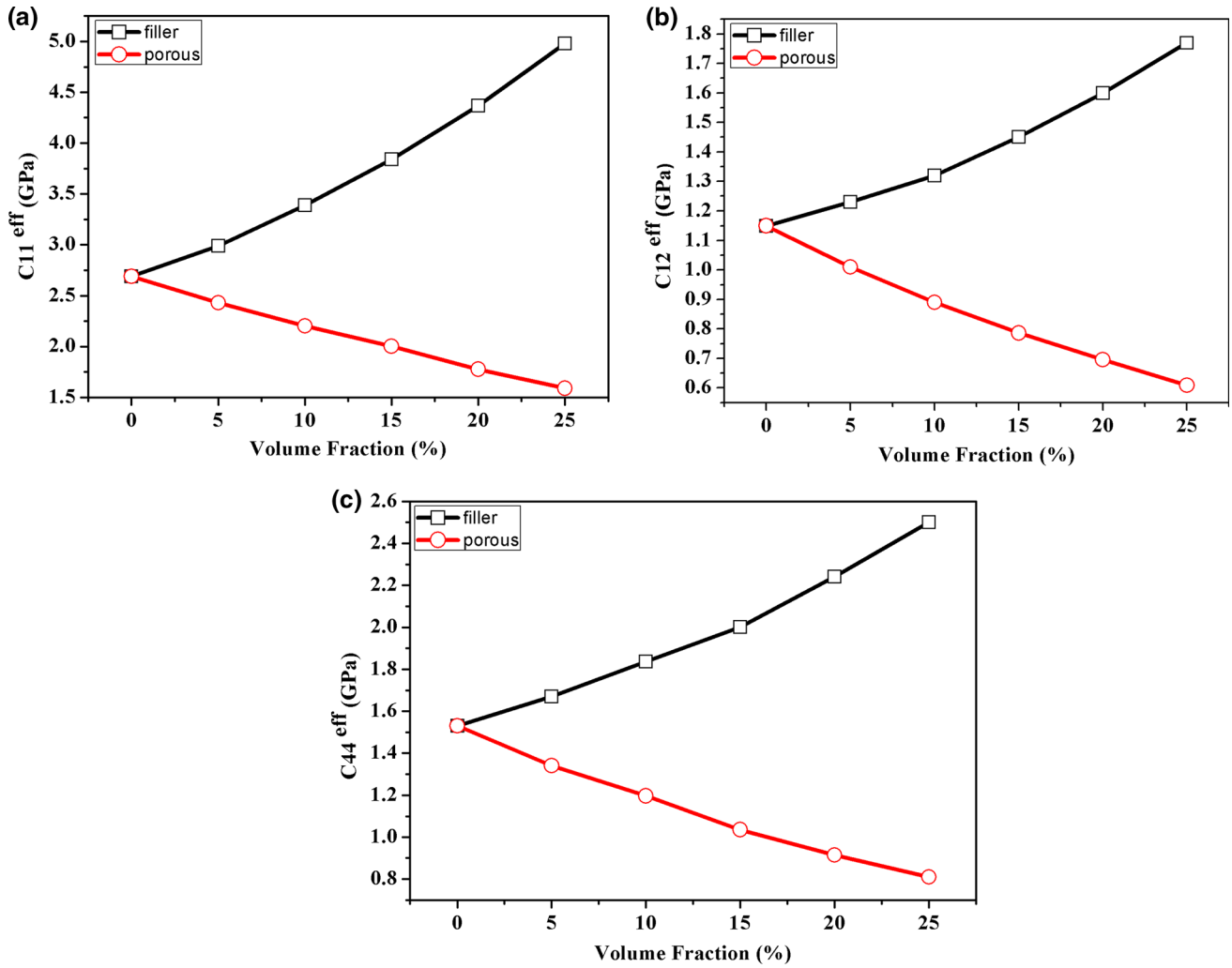

Fig. 3. Variation of (a) C_{11}^{eff}, (b) C_{12}^{eff}, and (c) C_{44}^{eff} with different volume fractions of filler and pores.

RESULTS AND DISCUSSION

The effective elastic, piezoelectric, and dielectric coefficients were computed for the 0–3 KNLNTS-PVDF composite and porous PVDF with different volume fractions of filler and porosity using the finite element method. It can be observed from Fig. 3a–c that the effective elastic constants increased as the volume fraction of KNLNTS particles was increased, but decreased as the porosity was increased. This trend can also be justified with the help of the rule of mixtures. Similarly, the effective piezoelectric coefficients presented in Fig. 4a–d show an increasing trend with filler volume fraction but decreased continuously as the porosity was increased.

These effective properties were further employed to characterize the sensing and energy harvesting behaviors of the cantilever beam. This analysis was carried out in the frequency domain on a cantilever beam with length of 100 mm, width of 25 mm, and thickness of 6 mm. To study the sensing characteristics, a tip load of 1 N was applied to the free end of the cantilever. The sensor open-circuit voltage was calculated using Eq. 25. The sensing voltage at the natural frequency of the system for composites filled with KNLNTS and porous PVDF is compared for different volume fractions in Fig. 5. It can be observed that the open-circuit voltage continuously increases with the volume fraction of the KNLNTS filler while for the porous ones it increases up to 15% volume fraction and then decreased. However, all the values for the porous materials remained lower than for pure PVDF. The variation in the sensing capability of the various composites in Fig. 5 can be understood by analyzing Eq. 25, which shows that the sensing voltage is directly proportional to e_{13}^{eff} but inversely proportional to $\varepsilon_{33}^{\text{eff}}$. For the filled composites, it can be observed from Fig. 4a and d that e_{13}^{eff} increased more rapidly than $\varepsilon_{33}^{\text{eff}}$. Meanwhile, for the porous materials, the ratio of e_{13}^{eff} to $\varepsilon_{33}^{\text{eff}}$ first increased up to 15%, then (due to the increased volume fraction of pores) e_{13}^{eff} decreased more rapidly than $\varepsilon_{33}^{\text{eff}}$, resulting in a drop in voltage.

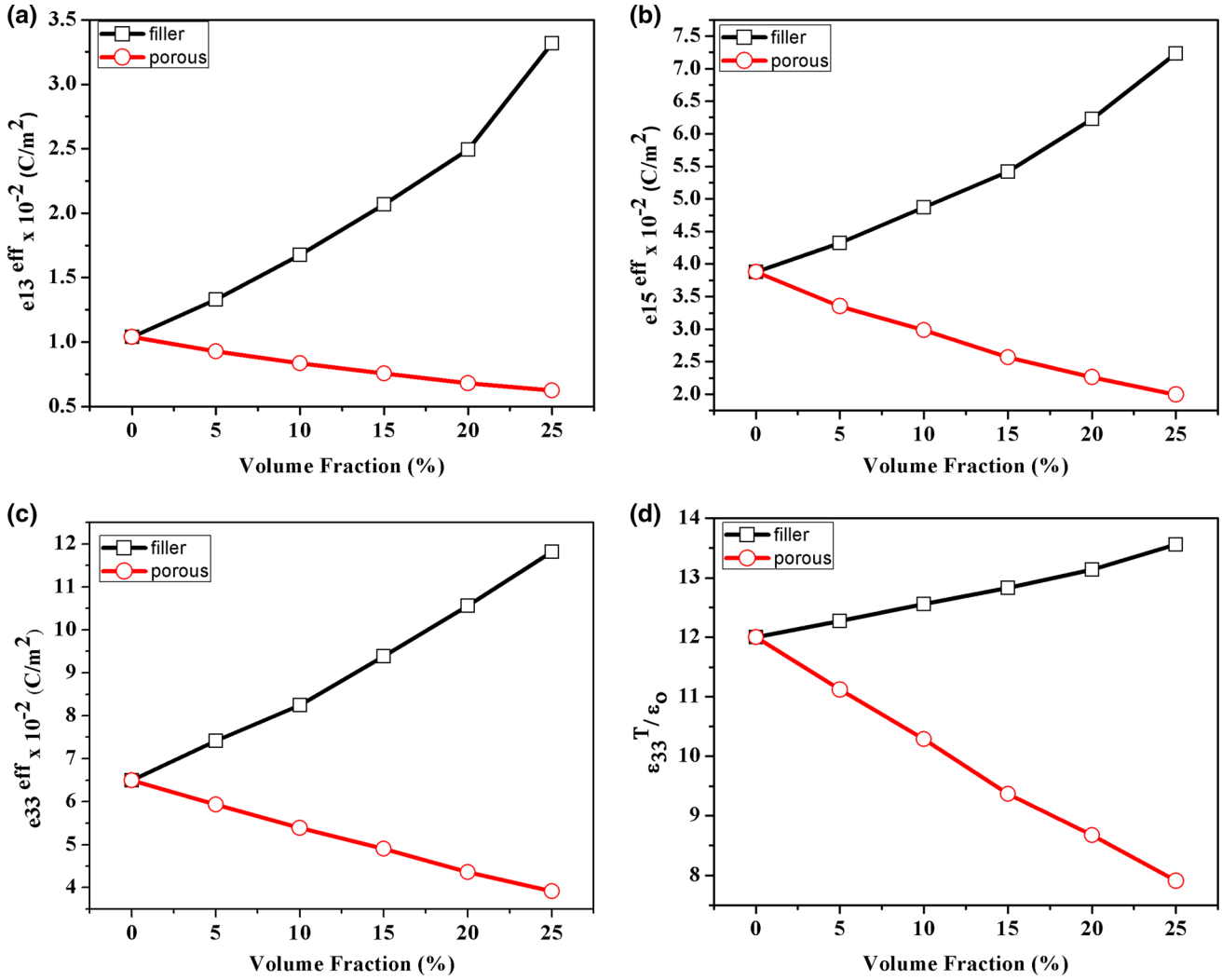

Fig. 4. Variation of (a) e_{13}^{eff}, (b) e_{15}^{eff}, (c) e_{33}^{eff}, and (d) $\varepsilon_{33}^{\text{eff}}$ with different volume fraction of filler and pores.

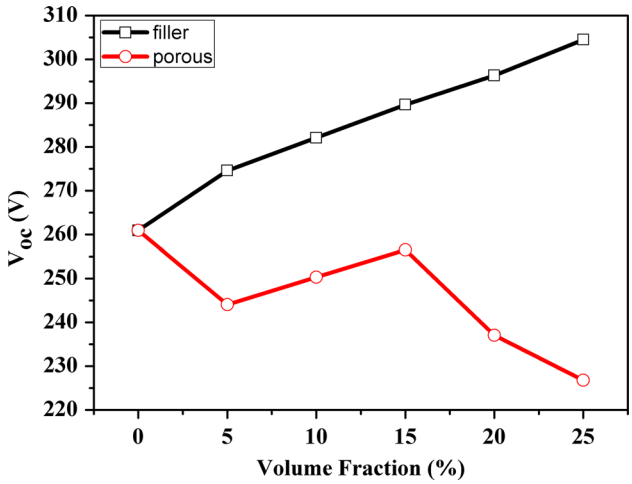

Fig. 5. Variation of maximum open-circuit voltage at resonant frequency for KNLNTS-filled composite and porous PVDF as function of volume fraction.

Furthermore, the voltage –frequency response was also studied for different volume fractions, for both the KNLNTS-filled composites and porous PVDF, as shown in Fig. 6. The variation in the natural frequency in both cases can be attributed to the density of the structure and the stiffness. The density increased continuously for the filled composites but decreased for the porous ones. Meanwhile, the stiffness depends on the effective elastic modulus of the material, which also increased continuously for the KNLNTS composites but decreased for the porous PVDF.

Cantilever beams are the most commonly used structures for piezoelectric energy harvesting from mechanical vibrations. The present study focused on the energy harvested using materials with different compositions. The effective material properties were used to predict the power produced by the piezocantilever under the action of a tip load of 1 N. The maximum power produced at the

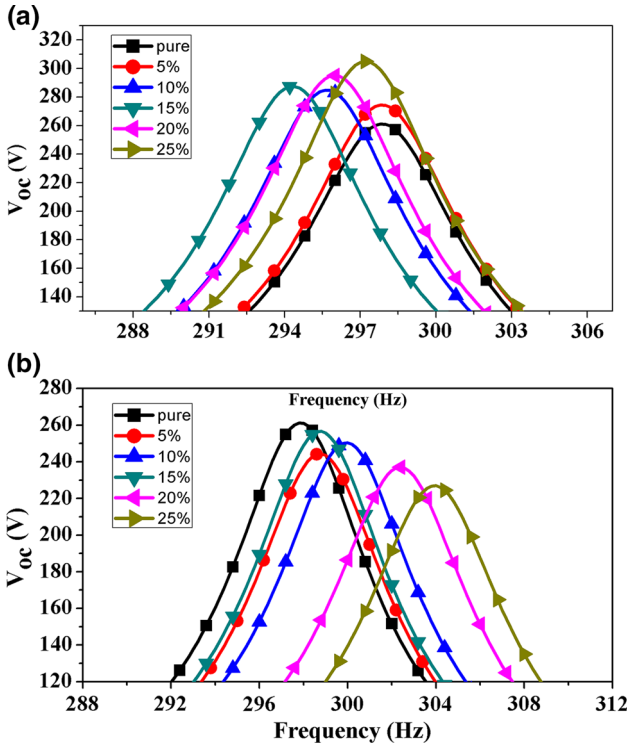

Fig. 6. Variation of open-circuit voltage for: (a) KNLNTS-filled composite and (b) porous PVDF as function of frequency.

fundamental natural frequency was computed. The optimum resistance required for the maximum output power was used, calculated as

$$R = \frac{1}{\omega C_{\mathrm{p}}}, \tag{31}$$

where ω is the natural frequency and C_{p} is the capacitance of the system.

Figure 7 shows that the power output follows the same pattern as the open-circuit voltage. For the KNLNTS composites, the power increased as the volume fraction was increased, while it first increased up to 15% volume fraction then decreased in the case of porous PVDF.

To validate the performance of the energy harvester, we calculated the figure of merit (FOM) for the filled and porous materials. The FOM proposed by Priya et al.[46] can be expressed as

$$\mathrm{FOM} = \frac{e_e^2}{E_e^2 \varepsilon_e}, \tag{32}$$

where e_e, E_e, and ε_e are the effective piezoelectric stress coefficient, effective elastic modulus, and effective dielectric constant, respectively, of the material. This FOM for the filled and porous PVDF with different volume fractions is shown in Fig. 8. It is observed that the trends in the voltage and output power are the same as that for the FOM. Therefore, it can be asserted that, although the voltage and

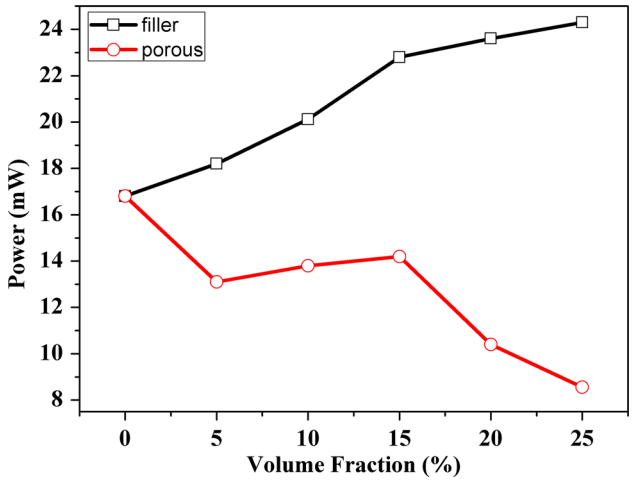

Fig. 7. Variation of maximum power produced by KNLNTS-filled composites and porous PVDF as function of volume fraction.

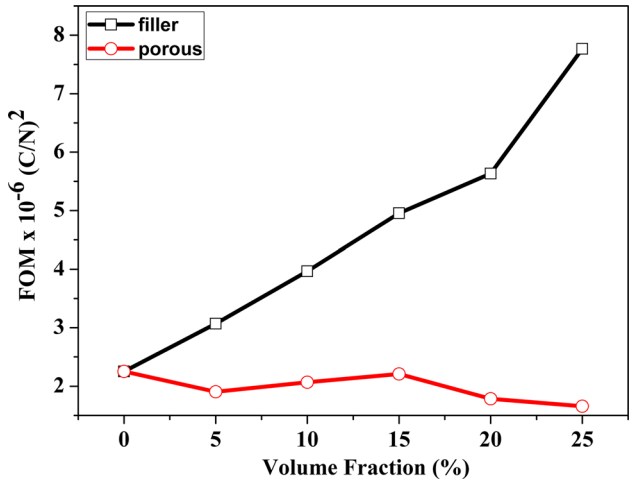

Fig. 8. Variation of FOM for KNLNTS-filled composites and porous PVDF as function of volume fraction.

power output depend on factors such as the boundary conditions and geometrical proportions of the cantilever used, their trends are the same, independent of the external force applied or beam shape used.

CONCLUSIONS

Finite element analysis of 0–3 polymer nanocomposites was carried out to determine the effective elastic and piezoelectric properties as functions of the volume fraction of KNLNTS filler or pores. The RVE was applied and suitable periodic boundary conditions imposed to simulate the composites for prediction of their effective properties. These properties were then used to predict the sensing and energy harvesting response of cantilever beams. It was found that the sensing voltage and power harvested using the filled composites increased, while for the porous composites these parameters increased up to a certain volume fraction then

decreased. It can therefore be concluded that piezoceramic-filled 0–3 composites could represent an alternative to bulk piezoceramics for use in sensing and harvesting applications where light weight is a primary concern.

ACKNOWLEDGEMENTS

R.V. acknowledges support from the Indian National Science Academy (INSA), New Delhi, India through a grant by the Department of Science and Technology (DST), New Delhi, India under the INSPIRE faculty award-2011 (ENG-01).

REFERENCES

1. N. Setter, *Piezoelectric Materials in Devices: Extended Reviews on Current and Emerging Piezoelectric Materials, Technology, and Applications* (Lausanne: EPFL, 2002), pp. 1–27.
2. S.R. Anton and H.A. Sodano, *Smart Mater. Struct.* 16, R1 (2007).
3. N. Hagood and A. Bent, in *AIAA/ASME/ASCE/AHS/ASC 34th Structures, Structural Dynamics, and Materials Conference* (1993), pp 3625-3638.
4. R. Newnham, D. Skinner, and L. Cross, *Mater. Res. Bull.* 13, 525 (1978).
5. M. Tabesh, A.M. Motlagh, and M. Elahinia, in *Proceedings of SPIE* (2009), pp 72880F-1-72880F-12.
6. K.-J. Yoon, K.-H. Park, S.-K. Lee, N.-S. Goo, and H.-C. Park, *Smart Mater. Struct.* 13, 459 (2004).
7. Y. Haddab, N. Chaillet, and A. Bourjault, in *Proceedings of the 2000 IEEE/RSJ International Conference on Intelligent Robots and Systems* (2000), pp 659-664.
8. D. Accoto, M. Carrozza, and P. Dario, *J. Micromech. Microeng.* 10, 277 (2000).
9. E. Aksel and J.L. Jones, *Sensors* 10, 1935 (2010).
10. M.D. Maeder, D. Damjanovic, and N. Setter, *J. Electroceram.* 13, 385 (2004).
11. T. Takenaka, H. Nagata, and Y. Hiruma, *Jpn. J. Appl. Phys.* 47, 3787 (2008).
12. Y. Saito, H. Takao, T. Tani, and T. Nonoyama, *Nature* 432, 84 (2004).
13. A. Kothari, A. Kumar, R. Kumar, R. Vaish, and V.S. Chauhan, *Polym. Compos.* 37, 1895 (2016).
14. K. Kwok, T. Lee, S. Choy, and H.L. Chan, *Lead-Free Piezoelectric Transducers for Microelectronic Wirebonding Applications* (Rijeka: InTech, 2010).
15. H. Berger, S. Kari, U. Gabbert, R. Rodriguez-Ramos, R. Guinovart, J.A. Otero, and J. Bravo-Castillero, *Int. J. Solids Struct.* 42, 5692 (2005).
16. A. Sharma, R. Kumar, R. Vaish, and V.S. Chauhan, *Int. J. Appl. Ceram. Technol.* 12, E64 (2015).
17. R. Kar-Gupta and T. Venkatesh, *Acta Mater.* 56, 3810 (2008).
18. Z. Wang, X. Jin, W. Chen, C. Zhang, C. Fu, and H. Gong, *Compos. Sci. Technol.* 105, 183 (2014).
19. R. Kar-Gupta and T. Venkatesh, *Acta Mater.* 54, 4063 (2006).
20. G. Martínez-Ayuso, M.I. Friswell, S. Adhikari, H.H. Khodaparast, and H. Berger, *Int. J. Solids Struct.* 113, 218 (2017).
21. T. Nestorović, D. Marinković, G. Chandrashekar, Z. Marinković, and M. Trajkov, *Finite Elem. Anal. Des.* 52, 11 (2012).
22. C. Poizat and M. Sester, *Comp. Mater. Sci.* 16, 89 (1999).
23. R.D. Medeiros, M.E. Moreno, F.D. Marques, and V. Tita, *J. Braz. Soc. Mech. Sci.* 34, 362 (2012).
24. P. Gaudenzi, *Comput. Struct.* 65, 157 (1997).
25. M.E. Moreno, V. Tita, and F.D. Marques, in *2009 Brazilian Symposium on Aerospace Eng. & Applications* (2009).
26. M. Melnykowycz, X. Kornmann, C. Huber, M. Barbezat, and A. Brunner, *Smart Mater. Struct.* 15, 204 (2006).
27. H.L.W. Chan and J. Unsworth, *IEEE Trans. Ultrason. Ferroelectr. Frequency Control* 36, 434 (1989).
28. W.A. Smith and B.A. Auld, *IEEE Trans. Ultrason. Ferroelectr. Frequency Control* 38, 40 (1991).
29. A. Bensoussan, J.-L. Lions, and G. Papanicolaou, *Asymptotic Analysis for Periodic Structures* (Amsterdam: North-Holland, 1978).
30. J. Bravo-Castillero, R. Guinovart-Díaz, F.J. Sabina, and R. Rodríguez-Ramos, *Mech. Mater.* 33, 237 (2001).
31. J.L. Teply and G.J. Dvorak, *J. Mech. Phys. Solids* 36, 29 (1988).
32. S. Nemat-Nasser and M. Hori, *Micromechanics: Overall Properties of Heterogeneous Materials* (Amsterdam: Elsevier, 2013).
33. H. Berger, S. Kari, U. Gabbert, R. Rodriguez-Ramos, J. Bravo-Castillero, R. Guinovart-Diaz, F. Sabina, and G. Maugin, *Smart Mater. Struct.* 15, 451 (2006).
34. P.M. Suquet, *Homogenization Techniques for Composite Media* (New York: Springer, 1987), p. 245.
35. V. Kouznetsova, M.G. Geers, and W.M. Brekelmans, *Int. J. Numer. Methods Eng.* 54, 1235 (2002).
36. N.S. Bakhvalov and G. Panasenko, *Homogenisation: Averaging Processes in Periodic Media: Mathematical Problems in the Mechanics of Composite Materials* (New York: Springer, 2012).
37. A. Agbossou, C. Richard, and Y. Vigier, *Compos. Sci. Technol.* 63, 871 (2003).
38. Z. Xia, Y. Zhang, and F. Ellyin, *Int. J. Solids Struct.* 40, 1907 (2003).
39. U. Galvanetto and M. Aliabadi, *Multiscale Modeling in Solid Mechanics: Computational Approaches* (Singapore: World Scientific, 2010).
40. S. Narayanan and V. Balamurugan, *J. Sound Vib.* 262, 529 (2003).
41. I.P. Correia, C.M.M. Soares, C.A.M. Soares, and J. Herskovits, *Comput. Struct.* 80, 2265 (2002).
42. C.-Y. Wang and R. Vaicaitis, *J. Sound Vib.* 216, 865 (1998).
43. X. Tan and L. Vu-Quoc, *Int. J. Numer. Methods Eng.* 64, 1981 (2005).
44. J. Kim, V.V. Varadan, and V.K. Varadan, *Int. J. Numer. Methods Eng.* 40, 817 (1997).
45. R. Kumar, B. Mishra, and S. Jain, *Finite Elem. Anal. Des.* 45, 13 (2008).
46. R.A. Islam and S. Priya, *Appl. Phys. Lett.* 88, 032903 (2006).